The Role of Zn in Chalcopyrite $CuFeS_2$: Enhanced Thermoelectric Properties of $Cu_{1-x}Zn_xFeS_2$ with In Situ Nanoprecipitates

Hongyao Xie, Xianli Su, Gang Zheng, Ting Zhu, Kang Yin, Yonggao Yan, Ctirad Uher, Mercouri G. Kanatzidis, and Xinfeng Tang**

Chalcopyrite ($CuFeS_2$) is a widespread natural mineral, composed of earth-abundant and nontoxic elements. It has been considered a promising n-type material for thermoelectric applications. In this work, a series of Zn-doped $Cu_{1-x}Zn_xFeS_2$ (x = 0–0.1) compounds are synthesized by vacuum melting combined with the plasma activated sintering process. The role of Zn in the chalcopyrite and its different effects on thermoelectric properties, depending on its concentration and location in the crystal lattice, are discussed. It is found that Zn is an effective donor which increases the carrier concentration and improves the thermoelectric properties of $CuFeS_2$. When the content of Zn exceeds the solubility limit, Zn partially enters the Cu sites and forms in situ ZnS nanophase. This, in turn, shifts the balance between the anion and cation species which is re-established by the formation of antisite Fe/Cu defects. Beyond maintaining charge neutrality of the structure, such antisite defects relieve the lattice strain in the matrix and increase the solubility of Zn further. The highest ZT value of 0.26 is achieved at 630 K for $Cu_{0.92}Zn_{0.08}FeS_2$, which represents an enhancement of about 80% over that of the pristine $CuFeS_2$ sample.

1. Introduction

Increased concerns, in the past two decades, regarding the environmental deterioration and the sustainability of energy resources have sparked a vigorous research activity to identify alternative, environmentally friendly energy sources and novel and efficient energy materials.[1–4] Owing to their ability to convert waste heat into electrical power, thermoelectricity has attracted a worldwide attention, and great progress has been made in improving existing thermoelectric materials and identifying novel efficient thermoelectric compounds.[5–17] As is well known, the efficiency of thermoelectric conversion depends on the dimensionless figure of merit $ZT = \alpha^2\sigma T/(\kappa_e + \kappa_L)$, where α is the Seebeck coefficient, σ is the electrical conductivity, T is the absolute temperature, and κ_e and κ_L are the electronic and lattice contributions to the thermal conductivity.[18,19] From this formula, it follows that a good thermoelectric material should have a large Seebeck coefficient, high electrical conductivity, and a low lattice thermal conductivity. Currently, the bulk of thermoelectric modules on the market use Bi_2Te_3-based[20–22] compounds for thermoelectric cooling devices and PbTe-based[5,6,8] compounds for power generation. Although their performance has been greatly improved compared to modules of 10–20 years ago, these compounds contain toxic (Pb) and very expensive (Te) elements. This contributes to their limited commercial applications. Thus, it is important to focus research efforts on developing new, efficient, inexpensive, and environmentally benign thermoelectric materials.

In that context, a series of thermoelectric materials with the diamond-like structure, such as Cu_2SnQ_3 (Q = Se, S)[23–25] and Cu_3SbQ_4 (Q = Se, S),[26–28] have attracted much attention, primarily due to their intrinsically low lattice thermal conductivity and good electronic properties. A canonical example here is a nontoxic chalcopyrite $CuFeS_2$[29–33] with its diamond-like structure and constituent elements widely abundant in the earth crust.

The crystal structure of $CuFeS_2$ can be considered as a double sphalerite cell with the S atom residing in the tetrahedral void formed by Cu and Fe atoms, as shown in **Figure 1**. Because of the intrinsic S vacancy defect, $CuFeS_2$ shows n-type semiconducting behavior with a band gap of about 0.53 eV.[32] Some controversy has emerged regarding the chemical valence of Cu and Fe in $CuFeS_2$. Some experiments show Cu being monovalent and Fe being trivalent,[34] while other investigations have concluded that $CuFeS_2$ is a mixture of two ionic states: $Cu^+Fe^{3+}S^{2-}{}_2$ and $Cu^{2+}Fe^{2+}S^{2-}{}_2$.[35] Because of the magnetic moment of Fe^{3+},

H. Y. Xie, Prof. X. L. Su, G. Zheng, T. Zhu, K. Yin, Prof. Y. G. Yan, Prof. X. F. Tang
State Key Laboratory of Advanced Technology for Materials Synthesis and Processing
Wuhan University of Technology
Wuhan 430070, China
E-mail: suxianli@whut.edu.cn; tangxf@whut.edu.cn
Prof. C. Uher
Department of Physics
University of Michigan
Ann Arbor, MI 48109, USA
Prof. M. G. Kanatzidis
Department of Chemistry
Northwestern University
Evanston, IL 60208, USA

DOI: 10.1002/aenm.201601299

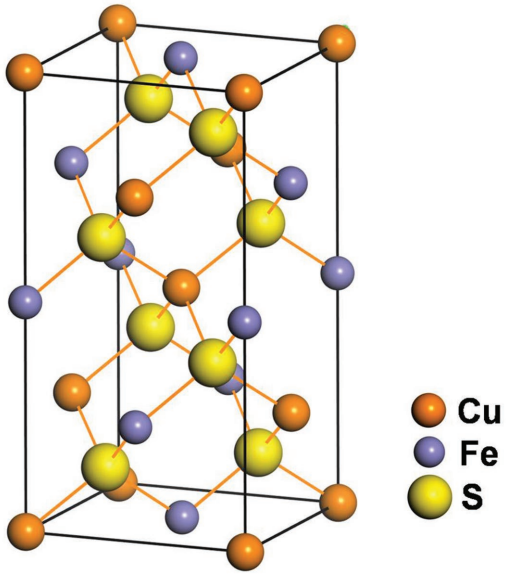

Figure 1. Crystal structure of $CuFeS_2$.

$CuFeS_2$ is an antiferromagnetic material with a Neel temperature of 823 K.[33] Some reports suggest that the d-orbitals of Fe hybridize with the sp-orbitals of S, resulting in an additional conduction band that straddles the fundamental broad energy gap near the valence band top.[36,37] The energy gap between the top of the valence band and the closest unfilled d conduction band is small, and imposes the temperature dependence on the carrier concentration.[37]

Although $CuFeS_2$ has a high Seebeck coefficient (around -480 μV K^{-1} at room temperature, partly due to the electron–magnon scattering),[32,38] combined with its low electrical conductivity and high thermal conductivity (due to its diamond-type structure), this leads to a low power factor and a rather low *ZT*. In order to optimize the electronic transport, the carrier concentration must be adjusted. Efforts along these lines have focused on controlling the chemical composition or on introducing element doping. Li et al.[29] used the deficiency of S to increase the carrier concentration in $CuFeS_{2-x}$. At the same time, the lattice thermal conductivity decreased on account of enhanced phonon scattering. Overall, a maximum *ZT* value of 0.21 was obtained at 573 K for $CuFeS_{1.8}$. Chen and co-workers[32] introduced antisite Fe/Cu defects in $Cu_{1-x}Fe_{1+x}S_2$ by changing the stoichiometric ratio. As a consequence, the carrier concentration and the electrical conductivity increased. Because such antisite defects enhance point defect scattering, the lattice thermal conductivity decreased concurrently. Maignan and co-workers[33] have improved the thermoelectric performance of $CuFeS_2$ by introducing Co as a dopant. Tsujii and Mori[30] have studied low-temperature thermoelectric properties of $Cu_{1-x}Fe_{1+x}S_2$ and $Cu_{1-x}Zn_xFeS_2$, and found that, unlike the case of Fe doping, Zn doping increases the carrier concentration but without any detrimental effect on the carrier mobility. As a result, they observed $Cu_{1-x}Zn_xFeS_2$ to have a higher power factor than $Cu_{1-x}Fe_{1+x}S_2$.

Although Zn appears as an effective dopant in $CuFeS_2$, its solubility in the crystal lattice of $CuFeS_2$ is limited. When more Zn is forced into the structure, Zn will combine with S to in situ form a ZnS secondary phase. Thus, there are competing modes of accommodation of Zn in $CuFeS_2$; Zn either dopes on the sites of Cu or forms a secondary phase. The presence of the secondary phase of ZnS changes the charge neutrality between the anion and cation species in favor of cations. To restore the balance between the two, some Fe atoms must seek an accommodation on the sites of Cu, giving rise to antisite defects. What influence such Fe/Cu antisite defects have on the lattice strain, and the electronic and thermal transport properties is of considerable interest regarding the eventual thermoelectric performance of the material. This, together with the fact that high-temperature transport measurements of $Cu_{1-x}Zn_xFeS_2$ have not been discussed in detail,[39] was the primary motivation for our study.

In this work, a series of $Cu_{1-x}Zn_xFeS_2$ (x = 0–0.1) compounds were synthesized by vacuum melting combined with the plasma activated sintering (PAS) process. The correlation between structure, microstructure, and transport properties was investigated. We found that the solubility of Zn in $CuFeS_2$ is low, and when the Zn content exceeds the solubility limit, Zn does two things: it enters the sites of Cu and it forms in situ ZnS which, in turn, leads to the formation of antisite defects of Fe/Cu. Such antisite defects relieve the lattice strain of the matrix, and this enhances the solubility of Zn further. The presence of the ZnS nanophase has a strong impact on the lattice thermal conductivity which is simulated using a model based on the effective medium approximation (EMA). The calculation shows that the radius of the ZnS nanoparticles has a crucial effect on the value of the lattice thermal conductivity of the composite $CuFeS_2$/ZnS structure. The thermoelectric performance of the $CuFeS_2$ compound can be improved by optimizing the amount of Zn dopants and modifying the morphology of the ZnS second phase.

2. Results and Discussion

2.1. Phase Composition and Microstructural Characterizations

Powder X-ray diffraction (XRD) patterns of nominal $Cu_{1-x}Zn_xFeS_2$ (x = 0, 0.01, 0.02, 0.03, 0.04, 0.06, 0.08, and 0.1) are shown in **Figure 2**a. For $x \leq 0.03$, the diffraction peaks are consistent with the standard pattern of $CuFeS_2$ (JCPDS#00-035-0752), indicating that these samples are single phases of $CuFeS_2$. When the content of Zn exceeded 0.03, XRD detected the presence of ZnS in the matrix, as shown in Figure 2b. The intensity of the ZnS signal increased with the increasing content of Zn. Judging by the XRD results, the solubility limit of Zn in $CuFeS_2$ is less than 0.03. The microstructure of sintered samples is shown in **Figure 3**a. When the content of Zn was less than 0.02, the grains were big and very clean with no precipitates being observed. When the Zn content reached 0.03, numerous nanoparticles emerged with sizes of 20–30 nm, uniformly distributed on smooth surfaces of the matrix grains. Increasing the content of Zn, the number of nanoparticles increased and their size grew. The energy dispersive spectrometer (EDS) result indicated these nanoparticles were composed of ZnS. Figure 3b shows the fracture

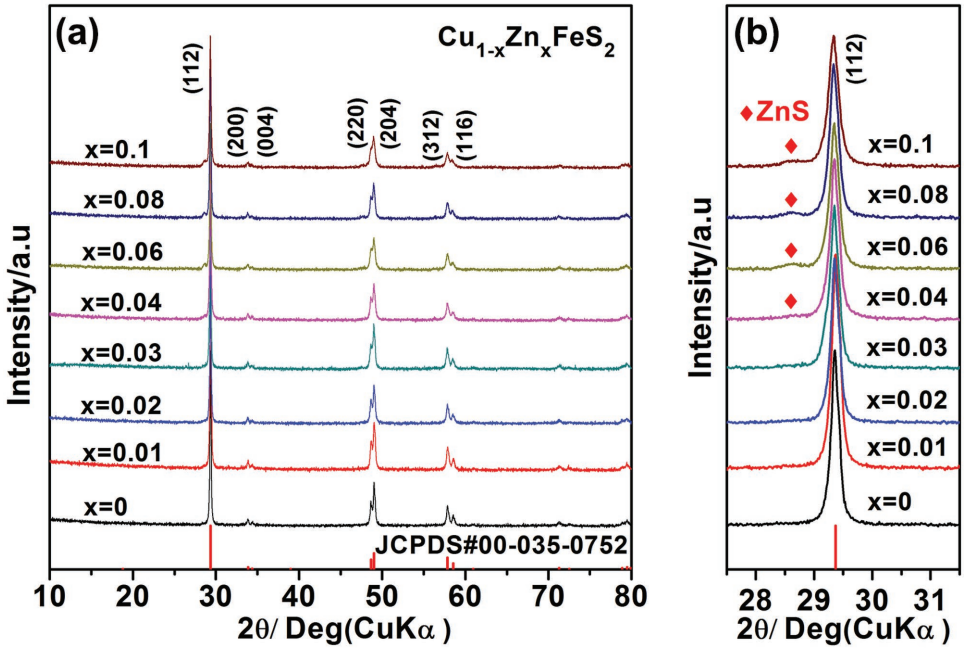

Figure 2. a) XRD patterns of PAS-sintered $Cu_{1-x}Zn_xFeS_2$ (x = 0, 0.01, 0.02, 0.03, 0.04, 0.06, 0.08, and 0.1). b) The main XRD peak as a function of composition x.

surface microstructure of the ingot before sintering. The ZnS nanoparticles are present and appear to be distributed in a layered fashion, suggesting they formed during the melting process.

We believe the layered structure of ZnS nanoparticles formed via a eutectic reaction[40,41] between ZnS and $CuFeS_2$. Although ZnS has a high melting point (2000 K), Zn will dissolve in $CuFeS_2$ when the melt is heated to 1323 K. Then, as

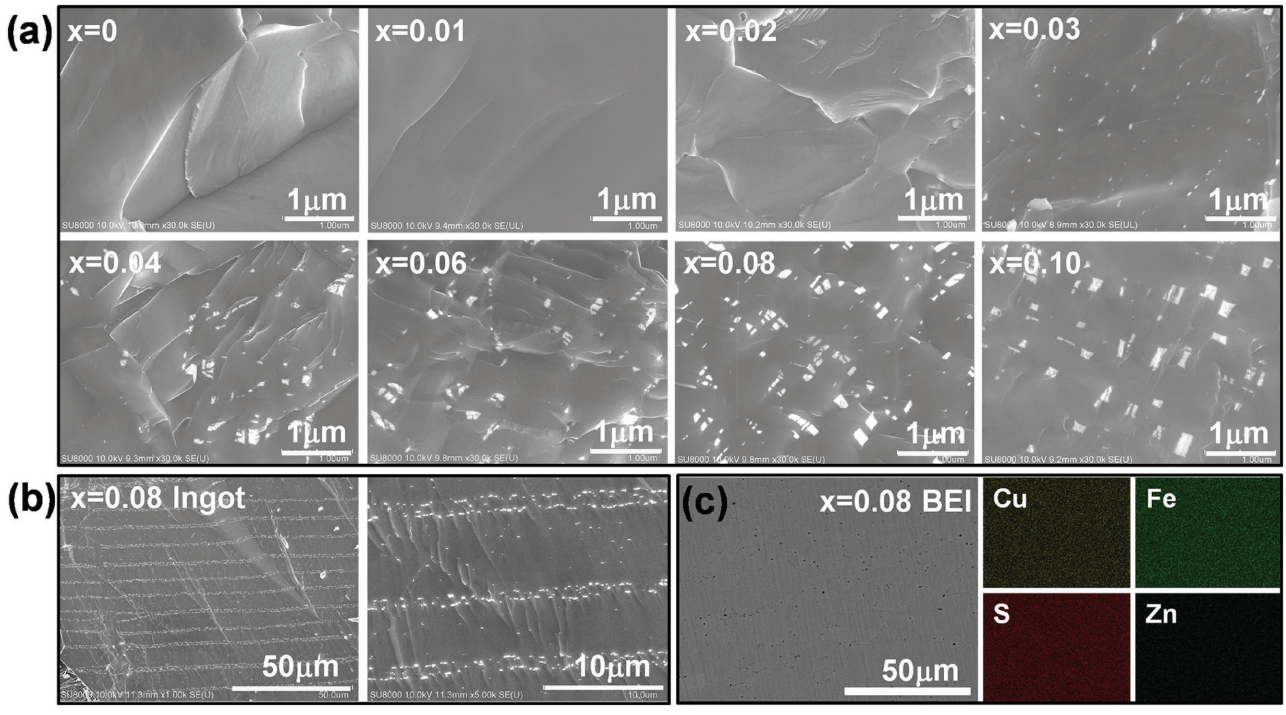

Figure 3. a) FESEM images of the free fracture surface of $Cu_{1-x}Zn_xFeS_2$ (x = 0, 0.01, 0.02, 0.03, 0.04, 0.06, 0.08, and 0.1). The light spots have been confirmed as ZnS by EDS analysis. b) FESEM images of the free fracture surface of the ingot of $Cu_{0.92}Zn_{0.08}FeS_2$ before sintering. c) BSE images of the polished surfaces and element maps by EDS for $Cu_{0.92}Zn_{0.08}FeS_2$.

the compound cools down, the solubility limit of Zn decreases, giving rise to in situ formed ZnS nanoparticles distributed in layers. The size of the ZnS nanoparticles grows rapidly as the content of Zn increases and reaches 200–300 nm at Zn concentrations higher than 0.04. The morphology of ZnS nanoparticles is the same in the ingot and in the sintered sample, meaning the ZnS nanoparticles are preserved following the process of sintering. Figure 3c shows a backscattered electron image (BEI) of the polished surface and element maps of $Cu_{0.92}Zn_{0.08}FeS_2$ obtained by EDS. No obvious large impurity phases are detected and the elements are distributed homogeneously. Because the ZnS nanoparticles are small and uniformly distributed in the matrix, it is difficult to detect them using BEI.

High-resolution transmission electron microscopy (HRTEM) was carried out to characterize the microstructure of two typical samples, $Cu_{0.97}Zn_{0.03}FeS_2$ and $Cu_{0.92}Zn_{0.08}FeS_2$ (the two structures contain different sizes of ZnS nanoparticles) as depicted in **Figure 4**. Figure 4a is a characteristic low magnification TEM image of the $Cu_{0.97}Zn_{0.03}FeS_2$ sample and it shows clearly the ZnS nanophase with an average size of 30 nm uniformly embedded in the matrix. An HRTEM image of the $Cu_{0.97}Zn_{0.03}FeS_2$ sample in Figure 4b shows one such ZnS nanoparticle. The calculated interplanar distance in this nanoparticle is 0.29 nm, consistent with the (101) planes of ZnS (JCPDS 00-005-0492). Figure 4c is a low-magnification TEM image of the $Cu_{0.92}Zn_{0.08}FeS_2$ sample, which shows three ZnS nanoparticles with the size of about 200 nm, consistent with the field emission scanning electron microscopy (FESEM) results. An HRTEM image of one of these ZnS nanoparticles is shown in Figure 4d. The nanoparticle is a polycrystalline entity with randomly oriented grains.

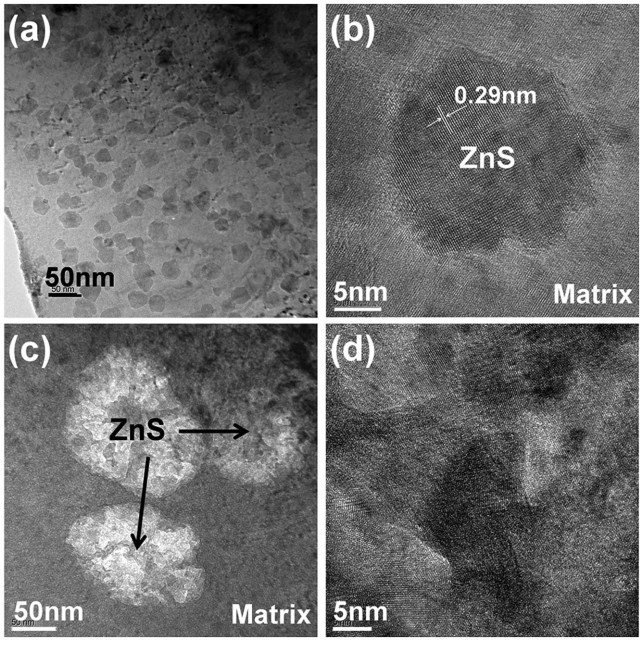

Figure 4. a) Low-magnification TEM image of $Cu_{0.97}Zn_{0.03}FeS_2$ showing high number density of ZnS nanoparticles. b) HRTEM image of a ZnS nanoparticle embedded in the $Cu_{0.97}Zn_{0.03}FeS_2$ sample. c) Low-magnification TEM image and d) HRTEM image, respectively, of ZnS particles in the $Cu_{0.92}Zn_{0.08}FeS_2$ sample.

2.2. The Form and Distribution of Zn Atoms

The XRD pattern and the FESEM result indicate that the solubility limit of Zn in $CuFeS_2$ is very small and, when the content of Zn exceeds 0.03, Zn tends to in situ form ZnS nanoparticles, uniformly dispersed in the matrix. However, according to the chemical formula, the stoichiometric ratio of Fe to Cu should be altered as the content of the ZnS second phase increases. This is due to a deficiency of S in the matrix as some fraction of S bonds with Zn, and the necessity to maintain balance between anion and cation species in the structure. The balance is achieved by Fe entering the sublattice of Cu, forming Fe/Cu antisite defects.

In order to reveal the effect of Zn on the matrix, an EDS has been used to probe the actual chemical composition of the matrix. The results are collected in **Table 1** and shown in **Figure 5**a as a plot of the nominal Zn content and the actual Zn/Fe molar ratio in the matrix. The red and blue lines represent the nominal and theoretical Zn/Fe molar ratios, respectively, and the black squares are the experimental values obtained by the EDS analysis. When the nominal Zn content is less than 0.03, all experimental values fall on the red line, indicating that Zn substitutes for Cu as a dopant. When the Zn content exceeds 0.03, experimental values deviate from the nominal Zn/Fe molar ratio (red line), because the Zn content has exceeded the solubility limit, and the excess fraction of Zn forms ZnS, as confirmed by the XRD and FESEM results. In theory, once the amount of Zn exceeds the solubility limit, the Zn/Fe molar ratio in the matrix should be constant and lies on the blue theoretical line. In reality, it keeps increasing (black squares). This suggests that a fraction of Zn continues to enter the matrix even though the Zn content is in excess of 0.03. A plausible reason for this to happen is as follows: radii of the elements in question follow a sequence Fe < Cu < Zn. When Zn substitutes for Cu, the crystal lattice expands and the lattice strain builds in. When the content of Zn is larger than 0.03, the strain exceeds the lattice tolerance and Zn in the matrix reaches the solubility limit. At this moment, the excess Zn starts to form the ZnS nanophase. Sulfur atoms bonding with Zn make the matrix deficient in S and, in order to maintain the balance between the anions and cations, some Fe atoms enter the Cu sublattice and form Fe/Cu antisite defects. Such Fe/Cu antisite defects will relieve the lattice strain in the matrix and, in turn, increase the solubility limit of Zn beyond 0.03. The trend in the lattice parameter and the carrier concentration (discussed later) provide support for the formation of Fe/Cu antisite defects.

The lattice parameters (*a*-axis and *c*-axis) of $Cu_{1-x}Zn_xFeS_2$ are shown in Figure 5b. Initially, the lattice parameter increases with the increasing Zn content. Then, as the content of Zn exceeds 0.03, the lattice parameter becomes constant. The trend is a result of the interplay between Zn doping and the formation of Fe/Cu antisite defects. Although both Zn and Fe enter the matrix (Fe in the form of Fe/Cu antisite defects), the lattice parameter remains constant due to the relationshipvamong the element radii (Fe < Cu < Zn).

In summary, Zn plays a dual role in the lattice of $Cu_{1-x}Zn_xFeS_2$. When its content is low (less than 0.03), Zn substitutes for Cu and acts as an effective donor. Once the content of Zn exceeds 0.03, Zn partially enters the matrix and also in situ forms the ZnS nanophase. The resulting alteration of

Table 1. Room temperature physical parameters of $Cu_{1-x}Zn_xFeS_2$ ($x = 0$, 0.01, 0.02, 0.03, 0.04, 0.06, 0.08, and 0.1).

Samples	Matrix composition	Zn/Fe [atomic ratio]	κ_L [W m^{-1} K^{-1}]	σ [10^4 S m^{-1}]	α [μV K^{-1}]	n_H [10^{19} cm^{-3}]	μ_H [cm^2 V^{-1} s^{-1}]	m^*/m_0
$x = 0.0$	$Cu_{25.38}Fe_{25.98}S_{48.64}$	0	8.42	0.53	−362	3.2	10.4	1.8
$x = 0.01$	$Cu_{25.05}Zn_{0.29}Fe_{26.03}S_{48.62}$	0.011	7.55	0.96	−292	9.7	6.2	3.1
$x = 0.02$	$Cu_{24.86}Zn_{0.50}Fe_{25.95}S_{48.69}$	0.019	6.86	1.40	−260	14.2	6.1	3.5
$x = 0.03$	$Cu_{24.52}Zn_{0.67}Fe_{26.01}S_{48.80}$	0.026	5.91	1.40	−244	17.4	5.0	3.8
$x = 0.04$	$Cu_{24.35}Zn_{0.84}Fe_{25.99}S_{48.82}$	0.032	6.63	2.27	−207	24.5	5.7	4.0
$x = 0.06$	$Cu_{23.85}Zn_{1.21}Fe_{26.06}S_{48.87}$	0.046	5.94	2.48	−191	32.1	4.7	4.4
$x = 0.08$	$Cu_{23.52}Zn_{1.54}Fe_{26.23}S_{48.71}$	0.058	5.28	2.42	−187	39.6	3.7	4.9
$x = 0.1$	$Cu_{23.03}Zn_{1.81}Fe_{26.3}S_{48.84}$	0.068	5.46	2.96	−170	49.5	3.7	5.2

the anion–cation balance is compensated by the formation of Fe/Cu antisite defects. Such antisite defects may relieve the lattice strain in the matrix and thus further increase the solubility of Zn. The sequence of events is illustrated through a chemical process

$$Cu_{1-x}Zn_xFeS_2 = \frac{1}{2}Cu_{1-\alpha}Zn_\alpha FeS_2 + \frac{1}{2}Cu_{1-\beta}FeS_{2-\beta} + \frac{\beta}{2}ZnS \quad (1)$$

This chemical formula can be modified into

$$Cu_{1-x}Zn_xFeS_2 = \frac{1}{2}Cu_{1-\alpha}Zn_\alpha FeS_2 + \frac{2-\beta}{4}Cu_{1-\gamma}Fe_{1+\gamma}S_2 + \frac{\beta}{2}ZnS \quad (2)$$

where

$$x = \frac{\alpha+\beta}{2}; \gamma = \frac{\beta}{2-\beta} \quad (3)$$

The room temperature carrier concentration and the carrier mobility are shown in Figure 5c. With the increasing Zn content, the carrier concentration increases linearly and the carrier mobility decreases. In order to calculate the carrier concentration quantitatively, the chemical valence of elements was studied using X-ray photoelectron spectroscopy (XPS). The results reveal the valence state of elements in $Cu_{1-x}Zn_xFeS_2$ as being Cu^+, Fe^{3+}, and Zn^{2+}. Hence, when Zn substitutes for Cu, it donates one electron to the matrix while when Fe forms an antisite defect it supplies two electrons. Through the analysis of the chemical composition, we know that when the Zn content exceeds 0.03, the chemical formula of "$Cu_{1-x}Zn_xFeS_2$" can be written as

$$\frac{1}{2}Cu_{1-\alpha}Zn_\alpha FeS_2 + \frac{2-\beta}{4}Cu_{1-\gamma}Fe_{1+\gamma}S_2 + \frac{\beta}{2}ZnS \quad (4)$$

Consequently, the increment of electrons in the material can be expressed as

$$\frac{\alpha}{2} + 2\times\frac{2-\beta}{4}\times\gamma = \frac{\alpha+\beta}{2} = x \quad (5)$$

This means, the carrier concentration only depends on the nominal Zn content, and this explains its linear dependence. Furthermore, the carrier concentration results provide support for the existence of Fe/Cu antisite defects.

In order to study the chemical state and shed light on the form of Zn in $Cu_{1-x}Zn_xFeS_2$, three samples with different Zn

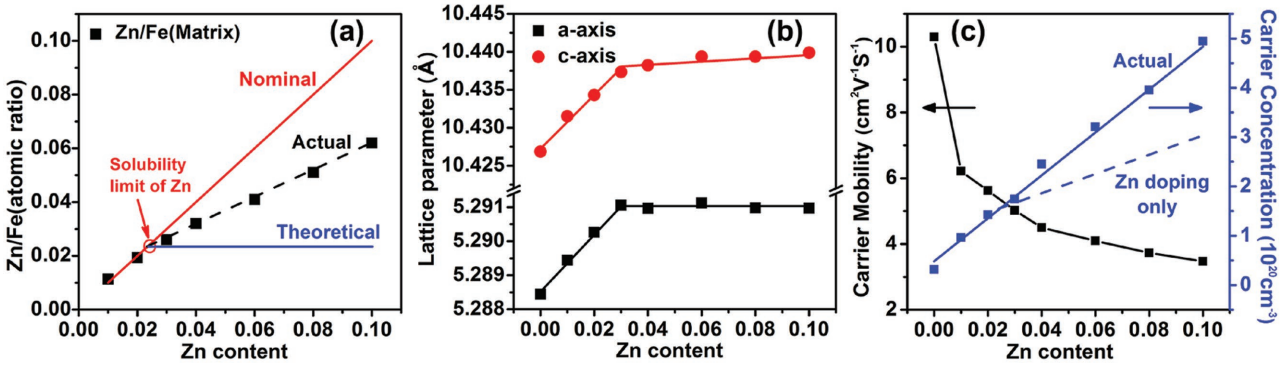

Figure 5. a) A relationship between the nominal Zn content and the actual Zn/Fe molar ratio in the matrix: the red line and the blue line represent the nominal and theoretical Zn/Fe molar ratios, respectively. b) Lattice parameters of $Cu_{1-x}Zn_xFeS_2$. c) Relationships between the nominal Zn content and the room temperature carrier concentration and carrier mobility: the solid blue line represents the actual carrier concentration while the dashed blue line indicates the carrier concentration expected when Zn was acting solely as a dopant.

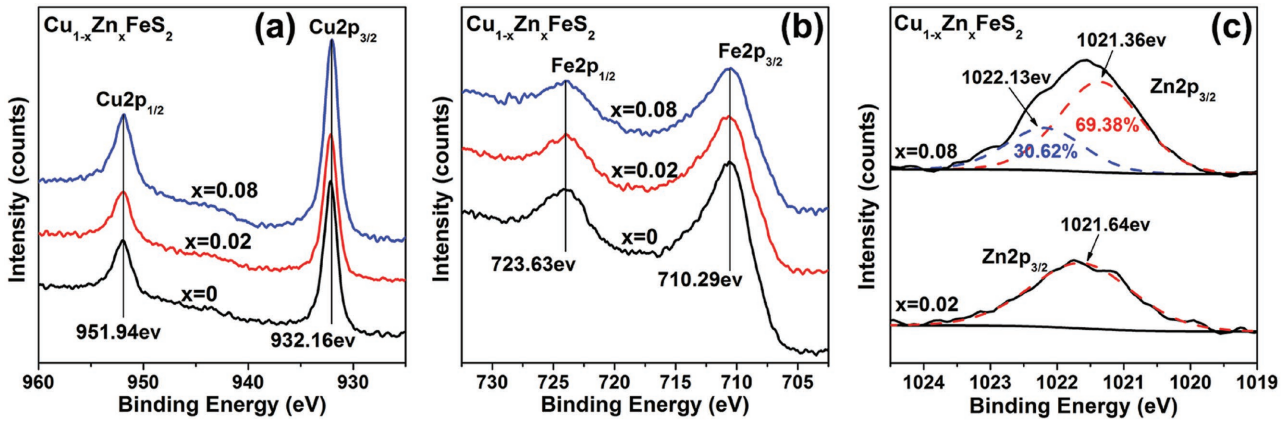

Figure 6. Photoemission spectra of a) Cu $2p_{1/2}$ and $2p_{3/2}$ core states, b) Fe $2p_{1/2}$ and $2p_{3/2}$ core states, and c) deconvolution spectra of Zn $2p_{3/2}$ core states in $Cu_{1-x}Zn_xFeS_2$ ($x = 0$, 0.02, 0.08) samples.

contents ($x = 0$, 0.02, and 0.08) were examined using XPS. The photoemission spectra of Cu $2p_{1/2}$ and $2p_{3/2}$ core states are shown in **Figure 6**a. No shake-up satellites at the high binding energy side of Cu $2p_{3/2}$ are observed, meaning that Cu has a full $3d^{10}$ shell and is monovalent (Cu^+) in $Cu_{1-x}Zn_xFeS_2$. Figure 6b shows the photoemission spectra of Fe $2p_{1/2}$ and $2p_{3/2}$ core states. Through the binding energy value and the valence of Cu, we can confirm that iron is in the Fe^{3+} state in $Cu_{1-x}Zn_xFeS_2$. The deconvoluted spectra of the Zn $2p_{3/2}$ core state are shown in Figure 6c. The results show that, for the $x = 0.02$ sample, Zn atoms are in only one chemical state. In contrast, the sample with the Zn content of $x = 0.08$ has two chemical states: the 1021 eV peak represents the doped fraction of Zn atoms, while the 1022 eV peak represents the state of Zn atoms in ZnS; their respective proportion is about 7:3, the value well corresponding to the EDS result.

2.3. Thermoelectric Performance

In the preceding sections, we have discussed the form and distribution of Zn in samples of "$Cu_{1-x}Zn_xFeS_2$" nominal composition. We now turn the attention to the effect of Zn and ZnS on the electrical and thermal transport properties in $Cu_{1-x}Zn_xFeS_2$. The room-temperature physical properties of all samples are summarized in Table 1. The lattice thermal conductivity decreases with increasing Zn content because of the enhanced phonon scattering caused by point defects and nanoparticles. The carrier concentration and the electrical conductivity increase with increasing Zn content, while the Seebeck coefficient and mobility decrease.

2.3.1. Electronic Transport Properties

Figure 7 depicts the temperature dependence of the electrical conductivity, the Seebeck coefficient, and the power factor of all samples. Because of the increasing carrier concentration, as shown in Table 1, the room-temperature electrical conductivity significantly increases from 5262 S m^{-1} for $CuFeS_2$ to 29 611 S m^{-1} for the sample with $x = 0.1$ of Zn (Figure 7a). This means that doping with Zn is an effective approach to enhance the electronic transport properties. For pure $CuFeS_2$, the electrical conductivity shows initially (300–450 K) a semiconductor behavior, while for samples doped with Zn, the electrical conductivity is much higher and it decreases monotonically with increasing temperature, consistent with degenerate semiconductor behavior. All samples exhibit negative

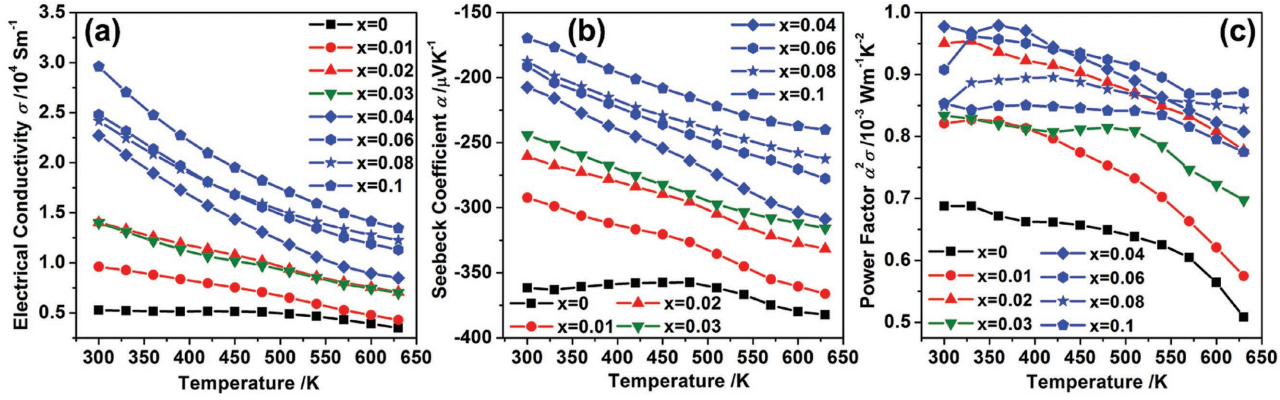

Figure 7. The temperature dependence of a) the electrical conductivity, b) the Seebeck coefficients, and c) the power factor for $Cu_{1-x}Zn_xFeS_2$ ($x = 0$, 0.01, 0.02, 0.03, 0.04, 0.06, 0.08, and 0.1).

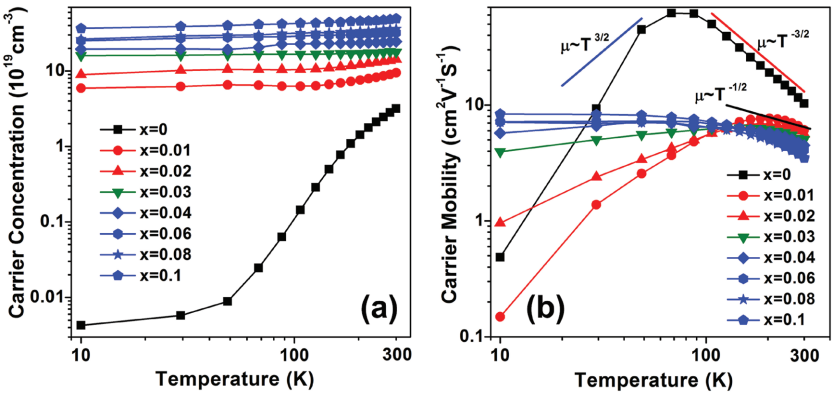

Figure 8. Temperature dependence (10–300 K) of a) the carrier concentration and b) the carrier mobility for $Cu_{1-x}Zn_xFeS_2$ ($x = 0$, 0.01, 0.02, 0.03, 0.04, 0.06, 0.08, and 0.1).

Seebeck coefficients over the entire temperature range (Figure 7b), documenting n-type character with electrons as the dominant charge carrier. In contrast with the behavior of the electrical conductivity, the absolute value of the Seebeck coefficient decreases with the increasing Zn content. The room-temperature Seebeck coefficient of pure $CuFeS_2$ is −361 μV K^{-1} and becomes −170 μV K^{-1} for the 0.1 Zn-doped sample. With increasing temperature, the absolute value of the Seebeck coefficient increases.

Any variation in the band structure and the Fermi level can be roughly deduced from the behavior of the electron effective mass. We estimate electron effective masses using a single parabolic band model and assuming that scattering is dominated by acoustic phonons. Then, the Seebeck coefficient is expressed as

$$\alpha = \frac{8\pi^2 k_B^2}{3eh^2}\left(\frac{\pi}{3n}\right)^{2/3} m^* T \tag{6}$$

where α is the Seebeck coefficient, k_B is the Boltzmann constant, h is the Planck constant, e is the electron charge, n is the carrier concentration, and m^* is the effective mass. Hence, the effective mass can be calculated from the experimental values of the Seebeck coefficient and the carrier concentration at 300 K. The results are shown in Table 1, and indicate that the effective mass of $CuFeS_2$ is increasing with the increasing content of Zn. Because of the increased electrical conductivity and the enhanced carrier effective mass, the Zn-doped samples achieve about 30%–40 % higher power factors compared to pristine $CuFeS_2$.

Temperature dependences of the carrier concentration and the carrier mobility in the interval of 10–300 K are shown in **Figure 8**. As we discussed above, the carrier concentration increases with the increasing Zn content because of the doping effect of Zn and the formation of Fe/Cu antisite defects which also act as effective donors. The carrier concentration of pristine $CuFeS_2$ is about 4.2×10^{16} cm^{-3} at 10 K and increases rapidly to 3.2×10^{19} cm^{-3} at 300 K, showing a distinctly semiconducting behavior. Research studies have indicated that the d-orbitals of Fe hybridize with the sp-orbitals of S and this leads to an additional conduction band appearing in the broad energy gap near the valence band top,[37] which gives rise to the temperature dependence of the carrier concentration. For the Zn-doped sample, the carrier concentration increases slightly with the increasing temperature, showing a degenerate semiconductor behavior.

For pristine synthetic samples of $CuFeS_2$, the carrier mobility follows the $T^{3/2}$ dependence in the temperature range of 10–100 K, indicative of ionized impurities dominating the carrier scattering. Such ionized impurities in the crystal lattice produce a long range Coulomb potential that strongly scatters electrons, leading to their low mobility in $CuFeS_2$. However, above 100 K, the temperature dependence changes to the $T^{3/2}$ variation, which suggests that the dominant carrier scattering process is acoustic phonon scattering. As the content of Zn increases, the carrier mobility decreases, and the carrier scattering mechanism at low temperatures changes from the one dominated by ionized impurity scattering to scattering dominated by neutral impurities. With the increasing temperature, the acoustic phonon scattering weakens as the Zn content increases and alloy scattering takes over.

2.3.2. Thermal Conductivity

Figure 9a shows the temperature dependence of the total thermal conductivity for all samples. As the temperature increases, the thermal conductivity of all samples decreases on account of the enhanced contribution of Umklapp processes. Figure 9b shows the temperature dependence of the lattice thermal conductivity. Because there is no sign of intrinsic excitations on any of the transport parameters, even at the highest temperature investigated, the bipolar thermal conductivity contribution to the total thermal conductivity must be very small, if any. We can thus estimate the lattice thermal conductivity by subtracting the electronic thermal conductivity from the measured total thermal conductivity

$$\kappa_L = \kappa - \kappa_e = \kappa - L\sigma T \tag{7}$$

where κ_L is the lattice thermal conductivity, κ is the total thermal conductivity, and κ_e is the electronic thermal conductivity, respectively. The latter can be estimated by the Wiedemann–Franz relation: $\kappa_e = L\sigma T$, where σ is the electrical conductivity and L is the Lorenz number. Assuming a single parabolic band model, the Lorenz number L is calculated from[42,43]

$$L = \left(\frac{k_B}{e}\right)^2 \left(\frac{(r+7/2)F_{r+5/2}(\eta)}{(r+3/2)F_{r+1/2}(\eta)} - \left[\frac{(r+5/2)F_{r+3/2}(\eta)}{(r+3/2)F_{r+1/2}(\eta)}\right]^2 \right) \tag{8}$$

Here, the reduced Fermi energy η can be obtained from the Seebeck coefficient as

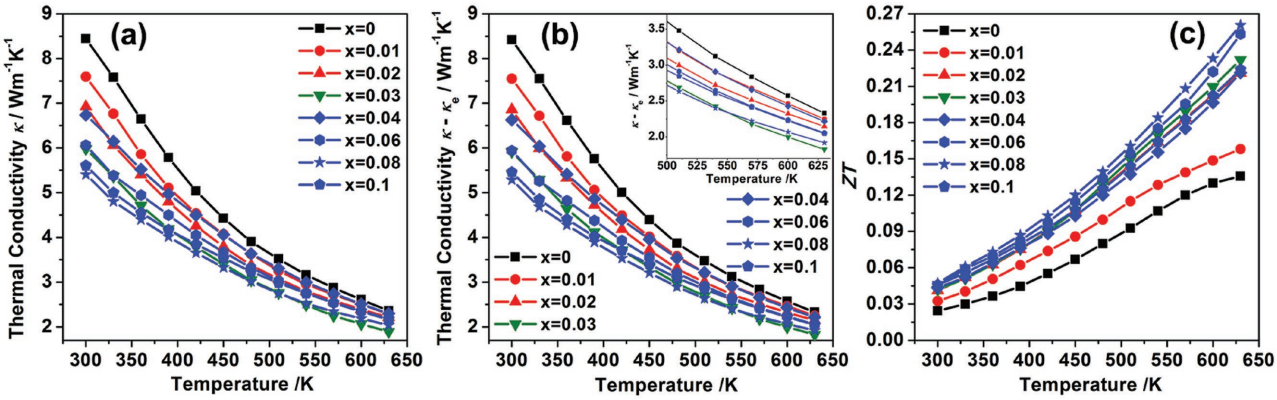

Figure 9. Temperature dependence of a) the total thermal conductivity, b) the lattice thermal conductivity, and c) the figure of merit *ZT* for $Cu_{1-x}Zn_xFeS_2$ (x = 0, 0.01, 0.02, 0.03, 0.04, 0.06, 0.08, and 0.1).

$$\alpha = \pm \frac{k_B}{e}\left(\frac{\left(r+\frac{5}{2}\right)F_{r+\frac{1}{2}}(\eta)}{\left(r+\frac{3}{2}\right)F_{r+\frac{1}{2}}(\eta)} - \eta\right) \quad (9)$$

$$F_n(\eta) = \int_0^\infty \frac{\chi^n}{1+e^{\chi-\eta}} d\chi \quad (10)$$

where k_B is the Boltzmann constant, e is the electron charge, α is the Seebeck coefficient, r is the scattering factor, here $r = -1/2$. Thus, obtained lattice thermal conductivity is shown in Figure 9b.

The room-temperature lattice thermal conductivity decreases with the increasing Zn content, from 8.5 W m^{-1} K^{-1} for pristine $CuFeS_2$ to 5.4 W m^{-1} K^{-1} for $Cu_{0.92}Zn_{0.08}FeS_2$. This indicates that Zn doping and ZnS nanoparticles are effective in scattering acoustic phonons. The enhanced electronic performance coupled with the decreased thermal conductivity results in an improved *ZT* value of 0.26 achieved at 630 K with $Cu_{0.92}Zn_{0.08}FeS_2$ (shown in Figure 9c). This represents about 80% enhancement over the value for the pristine $CuFeS_2$ sample.

We wish to point out an interesting behavior regarding the lattice thermal conductivity. **Figure 10** shows the room-temperature lattice thermal conductivity as it varies with the content of Zn. Three distinct regions are apparent, depending on the amount and form of Zn in $Cu_{1-x}Zn_xFeS_2$, as we discussed previously; low Zn content samples with x less than 0.03, where all Zn atoms substitute for Cu and act as electron donors; samples with the content of Zn in excess of 0.03, where Zn atoms partially enter the matrix, and also in situ form the ZnS nanophase which, in turn, leads to the formation of Fe/Cu antisite defects. Because the thermal conductivity of ZnS (κ_{ZnS} = 17.4 W m^{-1} K^{-1})[44] is much larger than that of pristine $CuFeS_2$ (κ_{CuFeS2} = 8.5 W m^{-1} K^{-1}), the overall thermal conductivity depends on the amount and form of Zn in the structure of $Cu_{1-x}Zn_xFeS_2$. Initially, Zn doping will increase the density of point defects in the lattice and decrease the lattice thermal conductivity as phonon scattering is enhanced. Then, as the content of Zn increases, a fraction of Zn atoms in situ form ZnS nanoparticles in the matrix which induces an interface thermal resistance that decreases the lattice thermal conductivity. On the other hand, due to the much higher thermal conductivity of ZnS nanophase, the total thermal conductivity of $Cu_{1-x}Zn_xFeS_2$ might increase when the ZnS nanoparticles grow larger and the interface between the two phases decreases. At that stage the sample becomes a mixture of two bulk phases. This competing trend is reflected in the behavior of the lattice thermal conductivity.

Below we discuss the effect of Zn doping and ZnS nanoparticles on the lattice thermal conductivity of $Cu_{1-x}Zn_xFeS_2$ and

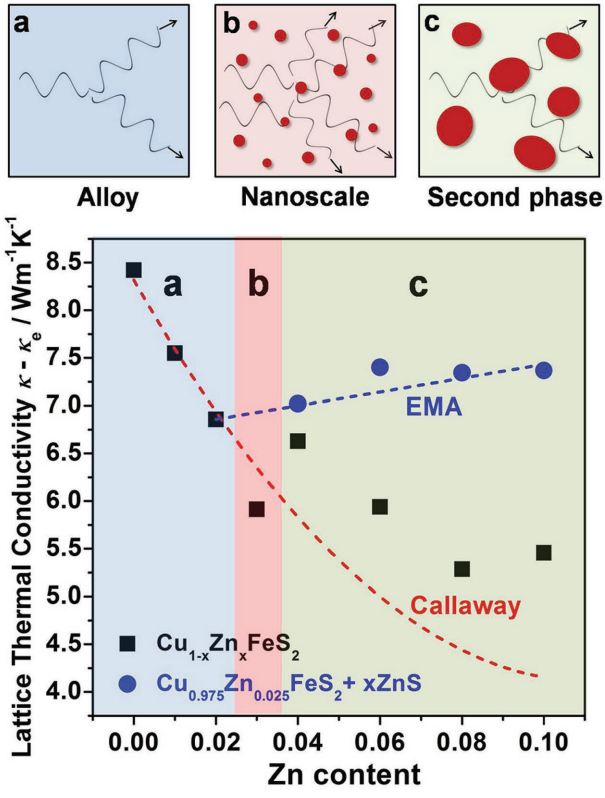

Figure 10. a–c) Room temperature lattice thermal conductivity of $Cu_{1-x}Zn_xFeS_2$ (x = 0, 0.01, 0.02, 0.03, 0.04, 0.06, 0.08, and 0.1) and of $Cu_{0.975}Zn_{0.025}FeS_2$ +xZnS (x = 0.015, 0.035, 0.055, and 0.075). (Bottom) The red line and the blue line are calculated results based on the Callaway model and the EMA model, respectively.

calculate its room temperature value using two distinct theoretical models: (1) the Callaway model to capture the dependence of the lattice thermal conductivity as a function of Zn doping. (2) The model based on the EMA to calculate the lattice thermal conductivity as a function of the fraction of ZnS nanoparticles present in the samples.

2.4. Different Influence of Zn and ZnS on the Lattice Thermal Conductivity

2.4.1. Influence of Zn Doping

We start with the Callaway[45,46] model and discuss the influence of Zn doping, i.e., point defects and alloying, on the thermal conductivity. Assuming the grain structure of all $Cu_{1-x}Zn_xFeS_2$ compounds with $x < 0.03$ is similar and grain boundary scattering is negligible, the scattering mechanisms governing heat transport are Umklapp processes and point defect scattering. Then, the relation between the lattice thermal conductivity of the disordered $Cu_{1-x}Zn_xFeS_2$ (κ_L) and that of the pure compound $CuFeS_2$ (κ_L^P) can be expressed as[47,48]

$$\frac{\kappa_L}{\kappa_L^P} = \frac{\tan^{-1} u}{u} \tag{11}$$

$$u^2 = \frac{\pi^2 \theta_D \Omega}{h v^2} \kappa_L^P \Gamma \tag{12}$$

where u is the disorder scaling parameter, θ_D is the Debye temperature, Ω is the average atomic volume, h is the Planck constant, v is the average sound velocity, and Γ is the scattering parameter. The scattering parameter can be calculated by the model of Slack[49] and Abeles,[50] taking $\Gamma = \Gamma_M + \Gamma_S$, where Γ_M and Γ_S are scattering parameters related to mass fluctuation and strain field fluctuation, respectively. They can be expressed as

$$\Gamma_M = \frac{\sum_{i=1}^{n} c_i \left(\frac{\overline{M_i}}{\overline{\overline{M}}}\right)^2 f_i^1 f_i^2 \left(\frac{M_i^1 - M_i^2}{\overline{M_i}}\right)^2}{\sum_{i=1}^{n} c_i} \tag{13}$$

$$\Gamma_S = \frac{\sum_{i=1}^{n} c_i \left(\frac{\overline{M_i}}{\overline{\overline{M}}}\right)^2 f_i^1 f_i^2 \varepsilon_i \left(\frac{r_i^1 - r_i^2}{\overline{r_i}}\right)^2}{\sum_{i=1}^{n} c_i} \tag{14}$$

where n is the number of different crystallographic sublattice types in the lattice and c_i are the relative degeneracies of the respective sites. For $CuFeS_2$, there are three different crystallographic sublattices: the Cu site, the Fe site, and the S site, so $n = 3$ and $c_1 = c_2 = 1$, $c_3 = 2$. $\overline{\overline{M}}$ is the average atomic mass of the compound, $\overline{M_i}$ and $\overline{r_i}$ are the average atomic mass and radius on the ith sublattice, respectively. Because there might be different types of atoms occupying any type of sublattices, and f^k_i will be the fractional occupation of the kth atoms on the ith sublattice, the atomic mass and radius are designated as M^k_i and r^k_i, respectively. The relations discussed above can be expressed as

$$\overline{M_i} = \sum_k f_i^k M_i^k \tag{15}$$

$$\overline{r_i} = \sum_k f_i^k r_i^k \tag{16}$$

$$\overline{\overline{M}} = \frac{\sum_{i=1}^{n} c_i \overline{M_i}}{\sum_{i=1}^{n} c_i} \tag{17}$$

Assuming all Zn atoms enter the Cu sublattice, the scattering parameter Γ can be written as

$$\Gamma = \frac{1}{4}\left(\frac{\overline{M_1}}{\overline{\overline{M}}}\right)^2 x(1-x)\left[\left(\frac{M_1^1 - M_1^2}{\overline{M_1}}\right)^2 + \varepsilon_1 \left(\frac{r_1^1 - r_1^2}{\overline{r_1}}\right)^2\right] \tag{18}$$

Therefore, the relationship between the lattice thermal conductivity of $Cu_{1-x}Zn_xFeS_2$ and the doping content of Zn can be predicted on the basis of the above calculation. The results are presented in **Table 2** and **Figure** 10 and **11**. The scattering parameters Γ_M and Γ_S, as a function of Zn doping content, are shown in Figure 11. The value of Γ_M is quite small due to a

Table 2. Disorder scattering parameters Γ_M, Γ_S, Γ, strain field-related adjustable parameter ε_1, disorder scaling parameter u, and the calculated lattice thermal conductivity for $Cu_{1-x}Zn_xFeS_2$ ($x = 0$, 0.01, 0.02, 0.03, 0.04, 0.06, 0.08, and 0.1).

Compound	Γ_M [10^{-3}]	Γ_S [10^{-3}]	Γ [10^{-3}]	ε_1	u	$\kappa_{L(calc)}$ [W m^{-1} K^{-1}]
$CuFeS_2$						8.42
$Cu_{0.99}Zn_{0.01}FeS_2$	0.004	4.712	4.716	452	0.615	7.55
$Cu_{0.98}Zn_{0.02}FeS_2$	0.008	10.083	10.091	489	0.900	6.86
$Cu_{0.97}Zn_{0.03}FeS_2$	0.012	16.090	16.102	526	1.137	6.29
$Cu_{0.96}Zn_{0.04}FeS_2$	0.015	22.707	22.722	562	1.350	5.82
$Cu_{0.94}Zn_{0.06}FeS_2$	0.023	37.676	37.699	636	1.739	5.08
$Cu_{0.92}Zn_{0.08}FeS_2$	0.029	54.799	54.828	710	2.098	4.52
$Cu_{0.9}Zn_{0.1}FeS_2$	0.037	73.881	73.918	783	2.436	4.08

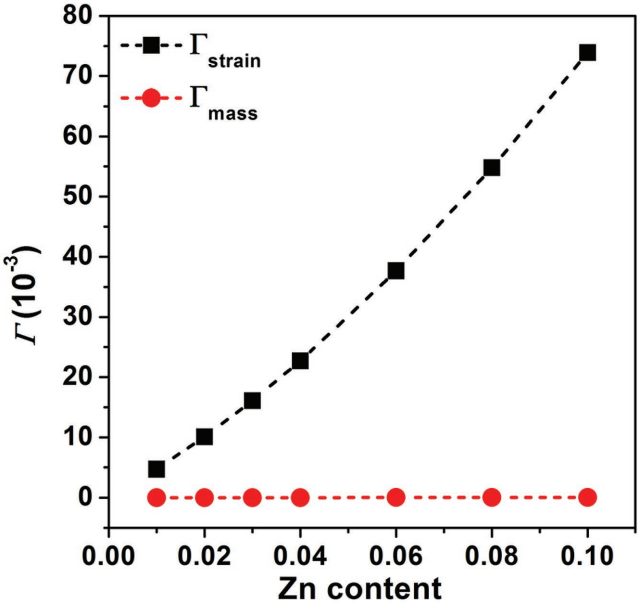

Figure 11. The mass fluctuation scattering parameter Γ_M and the strain field fluctuation scattering parameter Γ_S as a function of the content of Zn.

tiny mass difference between Zn and Cu; hence, mass fluctuation scattering is negligible. In contrast, the value of Γ_S is much larger, which implies that strain field fluctuations introduced by doping Zn on the Cu sublattice are the major contribution to phonon scattering and lead to a decrease in the lattice thermal conductivity.

Figure 10 shows the room-temperature lattice thermal conductivity as a function of Zn doping content. The black squares stand for the experimental value of $Cu_{1-x}Zn_xFeS_2$ and the red dashed line is the calculated result based on the Callaway model. As follows from the data, when the content of Zn is less than 0.03, the experimental lattice thermal conductivity is consistent with the calculated values. However, large deviations appear when the content of Zn exceeds 0.03. The experimental lattice thermal conductivity of the $Cu_{0.97}Zn_{0.03}FeS_2$ compound, i.e., $x = 0.03$, is notably lower than the calculated value for this composition, because the scattering processes are no longer limited to just Umklapp scattering and point defect scattering. Rather, the scattering of phonons is augmented by the presence of small ZnS nanoparticles (20–30 nm), leading to a low lattice thermal conductivity. When the content of Zn exceeds 0.04, the experimental lattice thermal conductivity becomes much larger than the calculated lattice thermal conductivity due to, now, much larger ZnS nanoparticles, effectively providing a thermal shunt. To investigate the size effect of ZnS nanoparticles on the lattice thermal conductivity, we turn to the EMA to analyze the lattice thermal conductivity.

2.4.2. Influence of ZnS Nanoparticles on the Lattice Thermal Conductivity

When the content of Zn reaches $x = 0.03$, the ZnS nanophase starts to appear in the matrix and the experimental lattice thermal conductivity deviates from the values calculated on the basis of the Callaway model. This is because of the high thermal conductivity and the increasing size of ZnS nanoparticles as the content of Zn increases. To analyze this situation, we model the thermal conductivity with the aid of the EMA.[44,51–53]

Based on EMA,[44,51] we are considering dispersed spherical particles of radius a of a material having the thermal conductivity K_p and occupying the volume fraction f, while being embedded in a matrix with the thermal conductivity K_m. The result for the effective thermal conductivity of the composite K^* can be expressed as follow

$$K^* = K_m \frac{K_P(1+2\alpha)+2K_m+2f\left[K_P(1-\alpha)-K_m\right]}{K_P(1+2\alpha)+2K_m-f\left[K_P(1-\alpha)-K_m\right]} \tag{19}$$

Here, α is the dimensionless parameter

$$\alpha = a_k/a \tag{20}$$

where a is the radius of the dispersed spherical particles and a_k is the Kapitza radius of the compound. According to the EMA theory, when the dispersed phase has a higher thermal conductivity than the matrix, the effective thermal conductivity of the composite depends on the relationship between the Kapitza radius and the distribution of particle radii. If the particles are smaller than the Kapitza radius, the effective thermal conductivity of the composite is lowered by the interface resistance. Whereas, if the particles are larger than the Kapitza radius, the high thermal conductivity of dispersed particles becomes significant and the effective thermal conductivity of the composite is increased (i.e., the sample is a physical mixture of two bulk phases). Therefore, the Kapitza radius is a critical parameter in the EMA theory, and it can be calculated as follows

$$a_k = R_{Bd}K_m;\ R_{Bd} = \frac{4}{\rho C v \eta} \tag{21}$$

Here, R_{Bd} is the boundary thermal resistance; ρ, C, and v are the density, specific heat, and Debye velocity of the matrix, respectively, and η is the average probability for the transmission of phonons across the interface into particles that can be expressed as $\eta = pq$, where p and q are parameters defined below. Because we ignore the effect of velocity dispersion and treat it as a constant to simplify the calculation, the value of R_{Bd} may be underestimated. We thus adjust the value by using a correction factor 2.3 from the literature.[51] The parameters p and q are given by

$$q = \frac{1}{2}\sin^2\theta_c = \frac{1}{2}\left(v/v'\right)^2 \tag{22}$$

$$p = \frac{4ZZ'}{(Z+Z')^2};\ Z = pv;\ Z' = p'v' \tag{23}$$

Hence, we can investigate the relationship between the lattice thermal conductivity of $Cu_{1-x}Zn_xFeS_2$ and the size of ZnS nanoparticles through the above calculation. The calculated results are shown in **Table 3**. For the $CuFeS_2$ matrix, the

Table 3. Room temperature physical parameters and EMA characteristic parameters for $CuFeS_2$ and ZnS.

Compound	ρ [kg m^{-3}]	V [m s^{-1}]	κ_L [W m^{-1} K^{-1}]	C [J kg^{-1} K^{-1}]	Z [10^7 kg m^{-2} s^{-1}]	p	q	η	R_{Bd} [10^{-9} K m^2 W^{-1}]	α_k [nm]
$CuFeS_2$	4170	2938	8.42	518	1.225	0.9975	0.3963	0.3953	3.667	31
ZnS	4100	3300	17.4	472	1.353					

Kapitza radius of ZnS is about 31 nm. Consequently, when the dispersed nanoparticles of ZnS are less than 31 nm, the thermal conductivity of $Cu_{1-x}Zn_xFeS_2$ is decreased due to the enhanced boundary scattering. In the opposite case, when ZnS nanoparticles are larger than 31 nm, the thermal conductivity of $Cu_{1-x}Zn_xFeS_2$ should increase. This explains the abnormal behavior of the thermal conductivity of $Cu_{1-x}Zn_xFeS_2$ when the content of Zn is 0.03. From FESEM and HRTEM results, we know that the sizes of ZnS nanoparticles are about 20–30 nm; hence, the thermal conductivity is decreased due to the "small" ZnS nanoparticles. However, when the content of Zn is larger than 0.04, the sizes of ZnS nanoparticles grow to about 200–300 nm, and now "big" ZnS nanoparticles will increase the thermal conductivity of $Cu_{1-x}Zn_xFeS_2$.

In order to examine the reliability of the conclusion obtained from the EMA model, the $Cu_{0.975}Zn_{0.025}FeS_2$ compound was loaded with different contents of ZnS, i.e., we synthesized composite structures of $Cu_{0.975}Zn_{0.025}FeS_2 + x$ZnS ($x$ = 1.5%, 3.5%, 5.5%, and 7.5%) and measured their thermal conductivity. We wish to point out that the size of ZnS nanoparticles was within 200–300 nm in all four composites. The results are shown in Figure 10. The first thing to note is that the experimental lattice thermal conductivity of $Cu_{1-x}Zn_xFeS_2$ (black square) is certainly lower than the experimental thermal conductivity of $Cu_{0.975}Zn_{0.025}FeS_2 + x$ZnS composite samples (blue circles). Moreover, the data also indicate that the calculated values of the thermal conductivity from the EMA model (blue dashed line) are consistent with the experimental values. This serves as the evidence of reliability of the EMA model and it also documents that the presence of ZnS nanoparticles with the size in the range of 200–300 nm definitely increases the thermal conductivity of $Cu_{1-x}Zn_xFeS_2$. It is important to keep in mind the difference between the Zn-doped $Cu_{1-x}Zn_xFeS_2$ samples and the composite $Cu_{0.975}Zn_{0.025}FeS_2 + x$ZnS samples. Although in the former structure, large (200–300 nm) ZnS nanoparticles increase the thermal conductivity, the deficiency of sulfur in the matrix gives rise to the formation of Fe/Cu antisite defects (to keep overall charge neutrality) that, by reducing the lattice strain, may enhance the solubility of Zn. No such effect is present in the case of $Cu_{0.975}Zn_{0.025}FeS_2 + x$ZnS samples, where the content of Zn in the matrix (x = 0.025) is low, no ZnS second phase can nucleate, and no Fe/Cu antisite defects form. It is due to the formation of Fe/Cu antisite defects and the ensuing enhanced solubility of Zn that the thermal conductivity of $Cu_{1-x}Zn_xFeS_2$ with $x > 0.03$ (black squares) is lower than that of composite $Cu_{0.975}Zn_{0.025}FeS_2 + x$ZnS samples (blue circles).

Our combined theoretical and experimental study of the thermal conductivity thus reveals that Zn doping and Fe/Cu antisite defects decrease the thermal conductivity of $Cu_{1-x}Zn_xFeS_2$ rather effectively. Moreover, when the in situ formed ZnS nanoparticles are less than 31 nm, which corresponds to the content of Zn of about 0.03, the thermal conductivity is further decreased due to enhanced boundary scattering of phonons. At a higher content of Zn, the nanoparticles attain sizes of 200–300 nm, well in excess of 31 nm, and such large nanoparticles increase the lattice thermal conductivity.

2.5. Zn Doping and the Influence of Fe/Cu Antisite Defects

The XRD and XPS results discussed above indicated that the $Cu_{0.98}Zn_{0.02}FeS_2$ compound (x = 0.02) is able to accommodate all Zn atoms and they exclusively substitute for Cu. Moreover, the respective valence states of the constituent elements are Cu^+, Zn^{2+}, and Fe^{3+}. Thus, when Zn substitutes for Cu, it donates one electron to the matrix while Fe forming an antisite Fe/Cu defect would donate two electrons. Consequently, the carrier concentration in $Cu_{0.98}Zn_{0.02}FeS_2$ and $Cu_{0.99}Fe_{1.01}S_2$ should be nominally the same. To compare the relative influence of Zn doping versus the influence of Fe/Cu antisite defects on the transport properties, we synthesized a $Cu_{0.99}Fe_{1.01}S_2$ compound and examined its transport behavior. Thus, making a comparative evaluation of two samples—$Cu_{0.98}Zn_{0.02}FeS_2$ and $Cu_{0.99}Fe_{1.01}S_2$—we can ascertain the influence of Zn and Fe at a nominally same carrier concentration level.

Room-temperature physical properties of the two samples are listed in **Table 4**. Indeed, while the carrier concentrations in $Cu_{0.98}Zn_{0.02}FeS_2$ and $Cu_{0.99}Fe_{1.01}S_2$ are very close, the Zn-doped sample has a higher mobility than the Fe-doped sample, even though the concentration of point defects induced by Zn is twice as much as that induced by Fe doping. The experimental result clearly indicates that Fe doping degrades the carrier mobility more strongly. The point is that Fe^{3+} carries a magnetic moment which scatters electrons very effectively and leads to a very low mobility.[30] Besides the effect on the carrier mobility, the Zn-doped sample also possesses a higher

Table 4. Room temperature physical parameters for $Cu_{0.98}Zn_{0.02}FeS_2$ and $Cu_{0.99}Fe_{1.01}S_2$.

Samples	σ [10^4 S m^{-1}]	α [μV K^{-1}]	n_H [10^{19} cm^{-3}]	μ_H [cm^2 V^{-1} s^{-1}]	γ [mJ mol^{-1} K^{-2}]	b [mJ mol^{-1} K^{-2}]	m_{dn}^*/m_0	Θ_D [K]
$Cu_{0.99}Fe_{1.01}S_2$	1.28	−239	13.8	5.7	0.709	0.33	2.3	287
$Cu_{0.98}Zn_{0.02}FeS_2$	1.40	−260	14.2	6.1	0.927	0.31	3.0	294

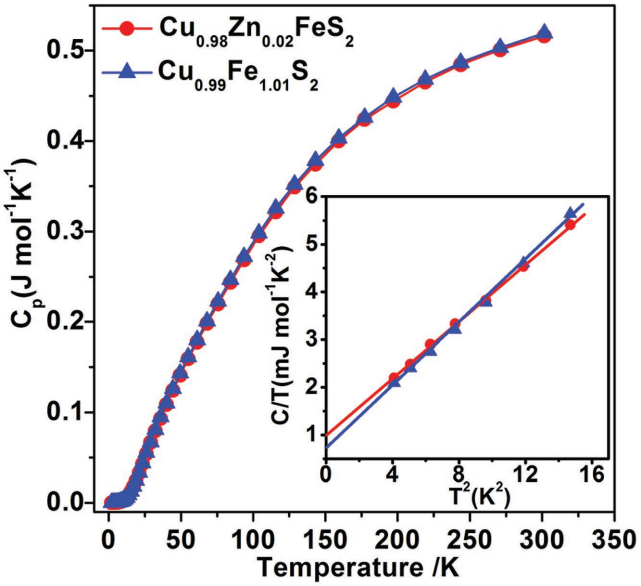

Figure 12. Low temperature specific heat C_p for $Cu_{0.98}Zn_{0.02}FeS_2$ and $Cu_{0.99}Fe_{1.01}S_2$. The inset shows the fitted curves of C_p/T versus T^2.

Seebeck coefficient than the Fe-doped sample. Because the density of states and effective mass at E_F can be roughly estimated through the low temperature heat capacity. In order to understand the variation of the Seebeck coefficient, the low temperature heat capacity C_p has been measured and the results are shown in **Figure 12**.

At low temperatures, the heat capacity can be expressed as $C_p = \gamma T + bT^3$, where bT^3 is the lattice contribution and γT is the contribution of electrons.[54] In the Debye model, $b = 12\pi^4 R/5\theta^3$, where θ is the Debye temperature and R is the molar gas constant. The linear coefficient γ is usually expressed as[55,56]

$$\gamma = \frac{\pi^2}{3} k_B^2 N(E_F) = 1.36 \times 10^{-4} \times V_{mol}^{2/3} n_\gamma^{1/3} \frac{m^*}{m_0} \quad (24)$$

Here, V_{mol} is the molar volume, n_γ is the number of electrons in the formula unit, m^* is the density of states effective mass, and m_0 is the mass of an electron. A plot of C_p/T versus T^2 should yield a straight line with the slope providing the value of b; see the inset in Figure 12, and the intercept with the ordinate at 0 K gives the value of γ. Thus obtained parameters b and γ were used to calculate the Debye temperature and the density of states effective mass based on the above equations.

The results for $Cu_{0.98}Zn_{0.02}FeS_2$ and $Cu_{0.99}Fe_{1.01}S_2$, the two samples with the same carrier concentration listed in Table 4, indicate that the Zn-doped sample has a higher density of states effective mass m^* than does the Fe-doped sample, and this is the reason for its higher Seebeck coefficient.

The temperature-dependent thermoelectric properties of the two samples are shown in **Figure 13**. The electrical conductivity in Figure 13a and the Seebeck coefficient in Figure 13b reveal that $Cu_{0.98}Zn_{0.02}FeS_2$ is superior to $Cu_{0.99}Fe_{1.01}S_2$, having both its electrical conductivity and the absolute value of the Seebeck coefficient larger throughout the whole temperature range investigated. This is consistent with the carrier mobility and effective mass results. At the same time, the thermal conductivity of the Zn-doped ($Cu_{0.98}Zn_{0.02}FeS_2$) sample is lower than that of the Fe-doped ($Cu_{0.99}Fe_{1.01}S_2$) sample due to the higher density of point defects and thus enhanced phonon scattering. Finally, due to the superior electrical performance and the lower thermal conductivity, the highest ZT value of 0.22 is achieved at 630 K for the Zn-doped sample. This represents about 50% enhancement over the Fe-doped sample having the same carrier concentration.

Because of the higher density of states mass and low magnetic scattering associated with Fe^{3+}, Zn-doped $CuFeS_2$ has the higher carrier mobility and Seebeck coefficient than the Fe-doped sample when they are at the same carrier concentration. Consequently, Zn-doped $CuFeS_2$ shows higher thermoelectric performance. If one could increase the solubility limit of Zn by using rapid synthetic methods, for example, melt-spinning[21,22] or self-propagating high temperature synthesis,[57–59] there is a good chance the thermoelectric performance of $CuFeS_2$ could be increased further.

3. Conclusion

The role of Zn added in the chalcopyrite lattice of $CuFeS_2$ on the structural and transport properties of the system is significant. We have shown that Zn is an effective donor that increases the carrier concentration and improves the thermoelectric properties of $CuFeS_2$. The solubility limit of Zn in $CuFeS_2$ is less than 3%. When the content of Zn exceeds this value, a fraction of Zn atoms enter the Cu sites and the remaining Zn atoms in situ form a uniformly distributed ZnS nanophase via a eutectic reaction between ZnS and $CuFeS_2$. In order to maintain the balance between anions and cations as some sulfur is bonding with Zn to form ZnS, a corresponding number of Fe atoms enter the Cu sublattice and form antisite defects. Such Fe/Cu antisite defects increase the carrier concentration and relieve the lattice strain in the matrix which, in turn, increases the solubility limit of Zn. A combined experimental and theoretical assessment shows that when the radii of ZnS nanoparticles are small, less than 31 nm, the lattice thermal conductivity is reduced due to the enhanced boundary scattering of phonons on ZnS nanoparticles. However, when the size of ZnS grows to 200 nm, as a consequence of the Zn content exceeding 3%, the lattice thermal conductivity increases, aided by the high thermal conductivity of ZnS. Finally, a comparative experimental study was made of the effect of Zn and Fe doping while keeping the same carrier concentration. The results clearly indicate that, compared to doping with Fe, doping with Zn is more effective in improving the thermoelectric properties of $CuFeS_2$. The discussion concerning the role of Zn and the formation and influence of the in situ formed ZnS nanophase is likely to be relevant to other Zn-doped, sulfur-based compounds. Clearly, the current method of synthesis seriously restricts the solubility limit of Zn in the chalcopyrite structure. We plan on overcoming this limitation by using far more rapid synthesis methods, hoping that this will dramatically enhance solubility of Zn in the crystal lattice and perhaps even alter the morphology of the ZnS secondary phase. If successful, further

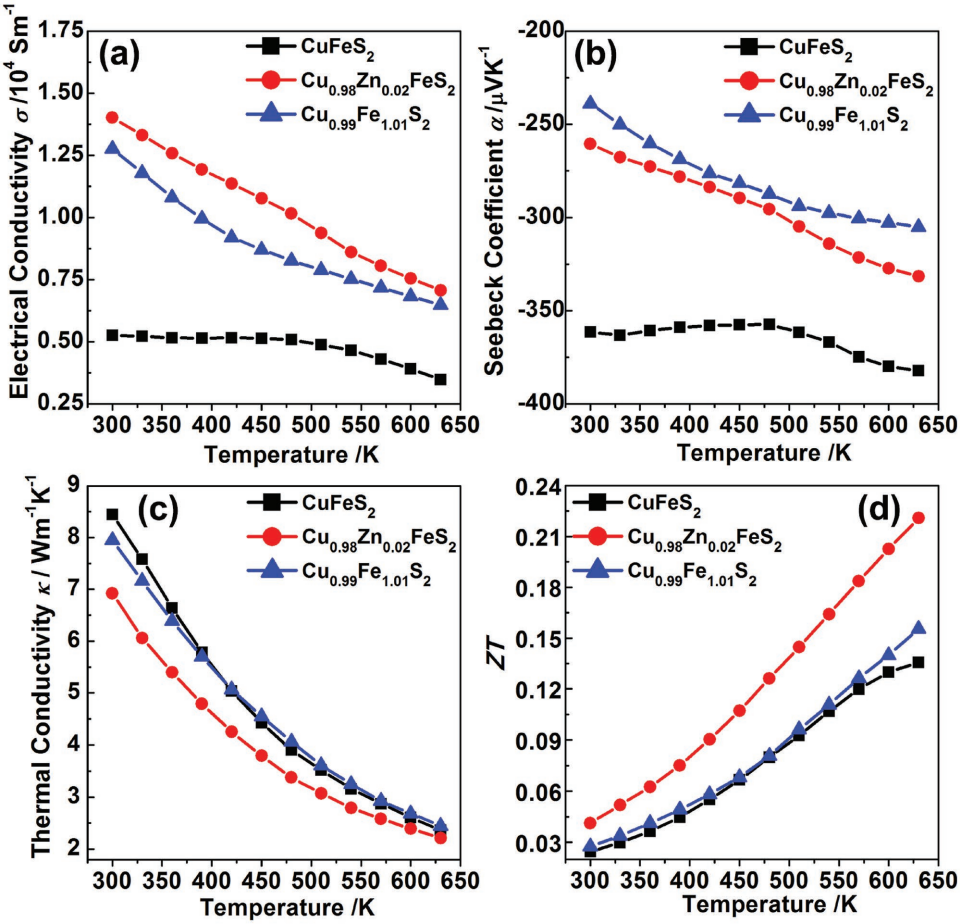

Figure 13. Temperature dependence of a) the electrical conductivity, b) the Seebeck coefficient, c) the thermal conductivity, and d) the figure of merit *ZT* for $CuFeS_2$, $Cu_{0.98}Zn_{0.02}FeS_2$, and $Cu_{0.99}Fe_{1.01}S_2$.

improvements in the thermoelectric performance of this inexpensive and environmentally friendly compound should follow.

4. Experimental Section

Compounds with the nominal composition of $Cu_{1-x}Zn_xFeS_2$ (x = 0, 0.01, 0.02, 0.03, 0.04, 0.06, 0.08, and 0.1) were synthesized by vacuum melting combined with the PAS process. High purity Cu (pieces, 99.99%), Fe (shot, 99.99%), Zn (pellet, 99.99%), and S (pieces, 99.99%) were weighted and mixed in stoichiometric proportions to achieve the desired composition (5 g). The mixtures were sealed in evacuated quartz tubes (diameter of 20 mm) and heated slowly up to 1323 K, kept at this temperature for 24 h, and then slowly cooled to room temperature. The obtained ingots were ground into fine powders and sintered using the PAS apparatus under a pressure of 40 MPa at 873 K for 5 min in a vacuum to obtain densified bulk samples (ϕ16 × 3.5 mm).

Powder XRD analysis (PANalytical–Empyrean; Cu K_α) was used to identify the purity and phase composition of the bulk samples. The morphology of the bulk samples was studied using FESEM (Hitachi SU8020) and HRTEM (JEM-2100F, JEOL). The chemical composition was obtained with the aid of an EDS (JXA-8230/INCAX-ACT). The chemical valence of elements was determined using XPS (VG Multilab 2000; Thermo Electron Corporation).

The electrical conductivity and the Seebeck coefficient were measured using a ZEM-3 apparatus (Ulvac Riko, Inc.) under a helium atmosphere from 300 to 630 K. The thermal conductivity was calculated from $\kappa = DC_p\rho$, where D is the thermal diffusivity measured in an argon atmosphere by the laser flash diffusivity method (LFA 457; Netzsch). The specific heat (C_p) was measured by a differential scanning calorimeter (DSC Q20; TA instrument) and the sample density (ρ) was determined by the Archimedes method. The electrical conductivity (σ), the Hall coefficient (R_H), and the low-temperature heat capacity (C) were measured using a Physical Property Measurement System (PPMS-9: Quantum Design). The carrier concentration (n) and the carrier mobility (μ_H) were calculated from $n = 1/eR_H$ and $\mu_H = \sigma/ne$. The overall accuracy of the measured *ZT* values was estimated to be about ±10%.

Acknowledgements

The authors thank Rong Jiang and Tingting Luo for help with the HRTEM analysis. The authors wish to acknowledge support from the National Basic Research Program of China (973 program) under project 2013CB632502, the Natural Science Foundation of China (Grant Nos. 51402222, 51172174, 51521001, and 51632006), and the 111 Project of China (Grant No. B07040). C.U. and X.T. also acknowledge support provided by the US–China CERC-CVC program under the Award Number DE-PI0000012. At Northwestern work is supported in part by a grant by the U.S. Department of Energy, Office of Science, and Office of Basic Energy Sciences under Award Number DE-SC000105 (M.G.K.).

Received: June 16, 2016
Revised: September 19, 2016
Published online: October 27, 2016

[1] J. R. Sootsman, D. Y. Chung, M. G. Kanatzidis, *Angew. Chem. Int. Ed.* **2009**, *48*, 8616.
[2] L. E. Bell, *Science* **2008**, *321*, 1457.
[3] T. M. Tritt, M. A. Subramanian, *MRS Bull.* **2006**, *31*, 188.
[4] M. S. Dresselhaus, G. Chen, M. Y. Tang, R. G. Yang, H. Lee, D. Z. Wang, Z. F. Ren, J. P. Fleurial, P. Gogna, *Adv. Mater.* **2007**, *19*, 1043.
[5] Y. Z. Pei, X. Y. Shi, A. LaLonde, H. Wang, L. D. Chen, G. J. Snyder, *Nature* **2011**, *473*, 66.
[6] Y. Z. Pei, A. F. May, G. J. Snyder, *Adv. Energy Mater.* **2011**, *1*, 291.
[7] J. P. Heremans, V. Jovovic, E. S. Toberer, A. Saramat, K. Kurosaki, A. Charoenphakdee, S. Yamanaka, G. J. Snyder, *Science* **2008**, *321*, 554.
[8] K. Biswas, J. Q. He, I. D. Blum, C. I. Wu, T. P. Hogan, D. N. Seidman, V. P. Dravid, M. G. Kanatzidis, *Nature* **2012**, *489*, 414.
[9] D. Wu, L. D. Zhao, S. Q. Hao, Q. K. Jiang, F. S. Zheng, J. W. Doak, H. J. Wu, H. Chi, Y. Gelbstein, C. Uher, C. Wolverton, M. Kanatzidis, J. Q. He, *J. Am. Chem. Soc.* **2014**, *136*, 11412.
[10] S. Perumal, S. Roychowdhury, D. S. Negi, R. Datta, K. Biswas, *Chem. Mater.* **2015**, *27*, 7171.
[11] C. G. Fu, S. Q. Bai, Y. T. Liu, Y. S. Tang, L. D. Chen, X. B. Zhao, T. J. Zhu, *Nat. Commun.* **2015**, *6*, 8144.
[12] H. H. Xie, H. Wang, Y. Z. Pei, C. G. Fu, X. H. Liu, G. J. Snyder, X. B. Zhao, T. J. Zhu, *Adv. Funct. Mater.* **2013**, *23*, 5123.
[13] X. Shi, J. Yang, J. R. Salvador, M. F. Chi, J. Y. Cho, H. Wang, S. Q. Bai, J. H. Yang, W. Q. Zhang, L. D. Chen, *J. Am. Chem. Soc.* **2011**, *133*, 7837.
[14] Y. T. Qiu, L. L. Xi, X. Shi, P. F. Qiu, W. Q. Zhang, L. D. Chen, J. R. Salvador, J. Y. Cho, J. H. Yang, Y. C. Chien, S. W. Chen, Y. L. Tang, G. J. Snyder, *Adv. Funct. Mater.* **2013**, *23*, 3194.
[15] L. D. Zhao, S. H. Lo, Y. S. Zhang, H. Sun, G. J. Tan, C. Uher, C. Wolverton, V. P. Dravid, M. G. Kanatzidis, *Nature* **2014**, *508*, 373.
[16] L. D. Zhao, G. J. Tan, S. Q. Hao, J. Q. He, Y. L. Pei, H. Chi, H. Wang, S. K. Gong, H. B. Xu, V. P. Dravid, C. Uher, G. J. Snyder, C. Wolverton, M. G. Kanatzidis, *Science* **2015**, *351*, 141.
[17] S. Q. Lin, W. Li, Z. W. Chen, J. W. Shen, B. H. Ge, Y. Z. Pei, *Nat. Commun.* **2016**, *7*, 10287.
[18] G. J. Snyder, E. S. Toberer, *Nat. Mater.* **2008**, *7*, 105.
[19] H. J. Goldsmid, *Introduction to Thermoelectric*, Springer, Heidelberg, Germany **2010**.
[20] B. Poudel, Q. Hao, Y. Ma, Y. C. Lan, A. Minnich, B. Yu, X. Yan, D. Z. Wang, A. Muto, D. Vashaee, X. Y. Chen, J. M. Liu, M. S. Dresselhaus, G. Chen, Z. F. Ren, *Science* **2008**, *320*, 634.
[21] W. J. Xie, J. He, H. J. Kang, X. F. Tang, S. Zhu, M. Laver, S. Y. Wang, J. R. D. Copley, C. M. Brown, Q. J. Zhang, T. M. Tritt, *Nano Lett.* **2010**, *10*, 3283.
[22] Y. Zheng, Q. Zhang, X. L. Su, H. Y. Xie, S. C. Shu, T. L. Chen, G. J. Tan, Y. G. Yan, X. F. Tang, C. Uher, G. J. Snyder, *Adv. Energy Mater.* **2014**, *5*, 1401391.
[23] X. Y. Shi, F. Q. Huang, M. L. Liu, L. D. Chen, *Appl. Phys. Lett.* **2009**, *94*, 122103.
[24] F. J. Fan, B. Yu, Y. X. Wang, Y. L. Zhu, X. J. Liu, S. H. Yu, Z. F. Ren, *J. Am. Chem. Soc.* **2011**, *133*, 15910.
[25] J. Fan, W. Schnelle, I. Antonyshyn, I. Veremchuk, W. Carrillo-Cabrera, X. Shi, Y. Grin, L. D. Chen, *Dalton Trans.* **2014**, *43*, 16788.
[26] T. R. Wei, H. Wang, Z. M. Gibbs, C. F. Wu, G. J. Snyder, J. F. Li, *J. Mater. Chem. A.* **2014**, *2*, 13527.
[27] L. Xi, Y. B. Zhang, X. Y. Shi, J. Yang, X. Shi, L. D. Chen, W. Zhang, J. H. Yang, D. J. Singh, *Phys. Rev. B.* **2012**, *86*, 155201.
[28] E. J. Skoug, J. D. Cain, D. T. Morelli, *Appl. Phys. Lett.* **2011**, *98*, 261911.
[29] J. H. Li, Q. Tan, J. F. Li, *J. Alloy Compd.* **2013**, *551*, 143.
[30] N. Tsujii, T. Mori, *Appl. Phys. Express.* **2013**, *6*, 043001.
[31] D. X. Liang, R. S. Ma, S. H. Jiao, G. S. Pang, S. H. Feng, *Nanoscale* **2012**, *4*, 6265.
[32] Y. L. Li, T. S. Zhang, Y. T. Qin, T. Day, G. Jeffrey Snyder, X. Shi, L. D. Chen, *J. Appl. Phys.* **2014**, *116*, 203705.
[33] D. Berthebaud, O. I. Lebedev, A. Maignan, *J. Materiomics* **2015**, *1*, 68.
[34] C. Boekema, A. M. Krupski, M. Varasteh, K. Parvin, F. van Til, F. van der Woude, G. A. Sawatzky, *J. Magn. Magn. Mater.* **2004**, *272–276*, 559.
[35] K. Sato, Y. Harada, M. Taguchi, S. Shin, A. Fujimori, *Phys. Status Solidi A.* **2009**, *206*, 1096.
[36] T. Oguchi, K. Sato, T. Teranishi, *J. Phys. Soc. Jpn.* **1980**, *48*, 123.
[37] V. V. Popov, P. P. Konstantinov, Y. V. Rud', *J. Exp. Theor. Phys.* **2011**, *113*, 683.
[38] R. Ang, A. U. Khan, N. Tsujii, K. Takai, R. Nakamura, T. Mori, *Angew. Chem. Int. Ed.* **2015**, *54*, 12909.
[39] N. Tsujii, T. Mori, Y. Isoda, *J. Electron. Mater.* **2014**, *43*, 2371.
[40] S. Gorsse, P. Bauer Pereira, R. Decourt, E. Sellier, *Chem. Mater.* **2010**, *22*, 988.
[41] T. Ikeda, E. S. Toberer, V. A. Ravi, G. J. Snyder, S. Aoyagi, E. Nishibori, M. Sakata, *Scr. Mater.* **2009**, *60*, 321.
[42] L. D. Zhao, S. H. Lo, J. Q. He, H. Li, K. Biswas, J. Androulakis, C. I. Wu, T. P. Hogan, D. Y. Chung, V. P. Dravid, M. G. Kanatzidis, *J. Am. Chem. Soc.* **2011**, *133*, 20476.
[43] W. S. Liu, Q. Y. Zhang, Y. C. Lan, S. Chen, X. Yan, Q. Zhang, H. Wang, D. Z. Wang, G. Chen, Z. F. Ren, *Adv. Energy Mater.* **2011**, *1*, 577.
[44] C. W. Nan, R. Birringer, D. R. Clarke, H. Gleiter, *J. Appl. Phys.* **1997**, *81*, 6692.
[45] J. Callaway, H. C. von Baeyer, *Phys. Rev.* **1960**, *120*, 1149.
[46] J. Callaway, *Phys. Rev.* **1959**, *113*, 1046.
[47] H. Wang, A. D. LaLonde, Y. Z. Pei, G. J. Snyder, *Adv. Funct. Mater.* **2013**, *23*, 1586.
[48] J. Yang, G. P. Meisner, L. Chen, *Appl. Phys. Lett.* **2004**, *85*, 1140.
[49] G. A. Slack, *Phys. Rev.* **1957**, *105*, 829.
[50] B. Abeles, *Phys. Rev.* **1963**, *131*, 1906.
[51] A. G. Every, Y. Tzou, D. P. H. Hasselman, R. Raj, *Acta Metall. Mater.* **1992**, *40*, 123.
[52] D. P. H. Hasselman, L. F. Johnson, *J. Compos. Mater.* **1987**, *21*, 508.
[53] R. L. Hamilton, O. K. Crosser, *Ind. Eng. Chem. Fundam.* **1962**, *1*, 187.
[54] E. S. R. Gopal, *Specific Heats at Low Temperatures*, Plenum Press, New York, USA **1966**.
[55] Q. Zhang, L. Cheng, W. Liu, Y. Zheng, X. L. Su, H. Chi, H. J. Liu, Y. G. Yan, X. F. Tang, C. Uher, *Phys. Chem. Chem. Phys.* **2014**, *16*, 23576.
[56] W. Liu, X. J. Tan, K. Yin, H. J. Liu, X. F. Tang, J. Shi, Q. J. Zhang, C. Uher, *Phys. Rev. Lett.* **2012**, *108*, 166601.
[57] X. L. Su, F. Fu, Y. G. Yan, G. Zheng, T. Liang, Q. Zhang, X. Cheng, D. W. Yang, H. Chi, X. F. Tang, Q. J. Zhang, C. Uher, *Nat. Commun.* **2014**, *5*, 4908.
[58] G. Zheng, X. L. Su, T. Liang, Q. B. Lu, Y. G. Yan, C. Uher, X. F. Tang, *J. Mater. Chem. A.* **2015**, *3*, 6603.
[59] T. Liang, X. L. Su, Y. G. Yan, G. Zheng, Q. Zhang, H. Chi, X. F. Tang, C. Uher, *J. Mater. Chem. A.* **2014**, *2*, 17914.